

Nitrogen-doped amorphous monolayer carbon

<https://doi.org/10.1038/s41586-024-07958-0>

Received: 29 November 2022

Accepted: 16 August 2024

Published online: 25 September 2024

 Check for updates

Xiuhibai^{1,7}, Pengfei Hu^{1,7}, Ang Li^{2,7}, Youwei Zhang^{1,7}, Aowen Li^{2,7}, Guangjie Zhang^{3,7}, Yufeng Xue^{4,7}, Tianxing Jiang¹, Zehou Wang¹, Hanke Cui¹, Jianxin Kang¹, Hewei Zhao¹, Lin Gu⁵✉, Wu Zhou²✉, Li-Min Liu⁴✉, Xiaohui Qiu^{3,6}✉ & Lin Guo¹✉

Monoatomic-layered carbon materials, such as graphene¹ and amorphous monolayer carbon^{2,3}, have stimulated intense fundamental and applied research owing to their unprecedented physical properties and a wide range of promising applications^{4,5}. So far, such materials have mainly been produced by chemical vapour deposition, which typically requires stringent reaction conditions compared to solution-phase synthesis. Herein, we demonstrate the solution preparation of free-standing nitrogen-doped amorphous monolayer carbon with mixed five-, six- and seven-membered (5-6-7-membered) rings through the polymerization of pyrrole within the confined interlayer cavity of a removable layered-double-hydroxide template. Structural characterizations and first-principles calculations suggest that the nitrogen-doped amorphous monolayer carbon was formed by radical polymerization of pyrrole at the α , β and N sites subjected to confinement of the reaction space, which enables bond rearrangements through the Stone–Wales transformation. The spatial confinement inhibits the C–C bond rotation and chain entanglement during polymerization, resulting in an atom-thick continuous amorphous layer with an in-plane π -conjugation electronic structure. The spatially confined radical polymerization using solid templates and ion exchange strategy demonstrates potential as a universal synthesis approach for obtaining two-dimensional covalent networks, as exemplified by the successful synthesis of monolayers of polythiophene and polycarbazole.

Introducing topological structures of non-hexagonal units into the honeycomb lattice can significantly alter the electronic and mechanical properties of sp^2 carbon networks, thus offering tunable properties akin to those of disordered hyperuniformity systems^{6–8}. Recent advances include synthesizing monolayer amorphous carbon consisting of mixed tiling of 5-6-7-8-membered rings using laser-assisted chemical vapour deposition (CVD)², in which carbon atoms produced from the decomposed gaseous precursor assemble into an amorphous lattice under conditions deviating from thermodynamic equilibrium. In another study, Tian et al. demonstrated precise control over the degree of disorder in monolayer amorphous carbon by adjusting the pyrolysis temperature in a low-temperature CVD process, thereby enabling modulation of the macroscopic electrical conductivity of the materials³.

Two-dimensional amorphous carbon networks also offer opportunities for investigating electron localization associated with the dopant chemistry. Incorporating heteroatoms into the strained carbon framework while maintaining the sp^2 fraction of the system provides a platform distinct from three-dimensional amorphous carbon, whose properties are typically explained by the Robertson model^{9–11}. However, a planar carbon structure with distorted rings is thermodynamically

metastable, posing a significant challenge for the controlled synthesis of such materials. The conventional high-temperature decomposition in CVD tends to favour C–C bond formation while suppressing the incorporation of dopants into the sp^2 carbon lattice^{12,13}.

Herein, we report the preparation of nitrogen-doped amorphous monolayer carbon (NAMC) using a space-confined solution-phase synthesis approach. We used nanosheets of layered double hydroxides (LDHs) as a removable template and an N-containing molecule as the precursor (Fig. 1a and Supplementary Figs. 1–6). Traditional solution-phase synthesis encounters hurdles in the preparation of free-standing carbon materials because of intricate interactions among building blocks, the spatial flexibility of the linked constituents and the poor solubility of reaction products. Templated reactions within the LDH interlayers¹⁴ or at substrate surfaces and air–liquid or liquid–liquid interfaces^{15–17} could circumvent these challenges by enforcing the in-plane arrangement and assembly of the building block, thus facilitating the subsequent construction of a covalent framework. Compared to CVD, this solution-based approach benefits from a wider selection of candidate precursors and holds promise for achieving the controlled incorporation of heteroatoms into the sp^2 carbon matrix, which is challenging for CVD because of the redox activity of the dopant atoms at

¹School of Chemistry, Beijing Advanced Innovation Center for Biomedical Engineering, Key Laboratory of Bio-Inspired Smart Interfacial Science and Technology, Beihang University, Beijing, China. ²School of Physical Sciences, University of Chinese Academy of Sciences, Beijing, China. ³CAS Key Laboratory of Standardization and Measurement for Nanotechnology, National Center for Nanoscience and Technology, Beijing, China. ⁴School of Physics, Beihang University, Beijing, China. ⁵Beijing National Center for Electron Microscopy and Laboratory of Advanced Materials, School of Materials Science and Engineering, Tsinghua University, Beijing, China. ⁶University of Chinese Academy of Sciences, Beijing, China. ⁷These authors contributed equally: Xiuhibai, Pengfei Hu, Ang Li, Youwei Zhang, Aowen Li, Guangjie Zhang, Yufeng Xue. ✉e-mail: lingu@tsinghua.edu.cn; wuzhou@ucas.ac.cn; liminliu@buaa.edu.cn; xhqliu@nanoctr.cn; guolin@buaa.edu.cn

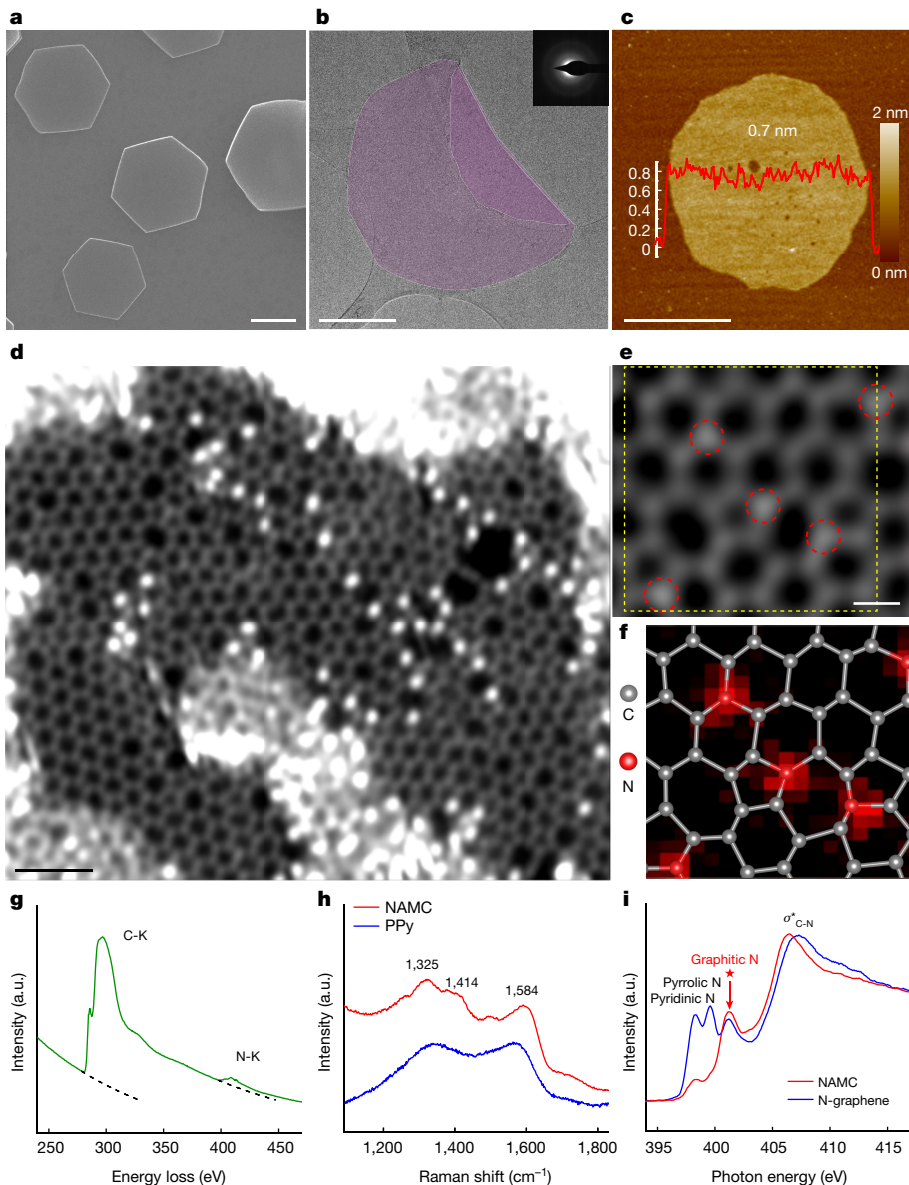


Fig. 1 | Structural characterization of the NAMC. **a**, Scanning electron microscope image of the LDH. Scale bar, 2 μm . **b**, TEM image of the NAMC after removing the LDH. Scale bar, 1 μm . Inset, Selected-area electron diffraction pattern of the NAMC. The colour overlay was added to facilitate identification of NAMC (purple). **c**, AFM image and the corresponding height profile of a NAMC flake. Scale bar, 500 nm. **d**, Atomic-resolution STEM-ADF image of NAMC. A few pinholes and small restacked nano-flakes can be observed. Scale bar, 1 nm. **e**, Representative high-magnification STEM-ADF image of NAMC. The N atoms, which have a slightly higher image contrast, are highlighted by

the red dashed circles. Scale bar, 0.2 nm. **f**, EELS map of N obtained from the area in **e** highlighted by the yellow box and overlaid with the corresponding atomic structural model. C and N atoms are represented by grey and red balls, respectively. **g**, EELS spectra acquired over a 32 nm \times 32 nm sample area for the C K-edge (C-K) and N K-edge (N-K). **h**, Raman spectra of the NAMC and PPy. **i**, Experimental N K-edge NEXAFS spectra of the NAMC and N-doped graphene. The peak for graphitic N (401.2 eV) is marked by the red star. The peaks around 398.3 and 399.6 eV are ascribed to pyridinic and pyrrolic N, respectively. a.u., arbitrary units.

high temperature. We demonstrate the versatility of this confined growth method by further synthesis of two-dimensional amorphous monolayers of polythiophene (PTH) and polycarbazole (PCZ).

In our work, persulfate ($\text{S}_2\text{O}_8^{2-}$) was adopted as the initiator and intercalated into the LDH interlayer through anion exchange with CO_3^{2-} (Supplementary Figs. 7 and 8), which takes advantage of the lamellar structure of LDH templates. It is crucial to thoroughly remove residual $\text{S}_2\text{O}_8^{2-}$ from the surfaces of LDH through rinsing and from the aqueous solution before polymerization to avoid surface and in-solution polymerization. The polymerization of the pyrrole is then strictly confined within the subnanometre interlayer of LDH (Supplementary Figs. 9 and 10). After removing the LDH template, the as-prepared samples show a homogeneous morphology with an average lateral size of over

1 μm , as shown by the transmission electron microscopy (TEM) image in Fig. 1b. A diffuse halo is seen in the selected-area electron diffraction pattern of the NAMC sample, suggesting an amorphous nature. Atomic force microscopy (AFM) measurements further show that the NAMC dispersed on mica exhibits a thickness of approximately 0.7 nm (Fig. 1c). This value is comparable to the thickness of single-layered graphene, indicating the monoatomic thickness of the NAMC sample.

Aberration-corrected scanning transmission electron microscopy (STEM) imaging combined with electron energy loss spectroscopy (EELS) was used to analyse the atomic structure of NAMC. The annular dark-field (ADF) images reveal a monoatomic-thick two-dimensional network consisting of distorted 5-6-7-membered rings with occasional 8-membered rings (Fig. 1d,e and Extended Data Figs. 1 and 2),

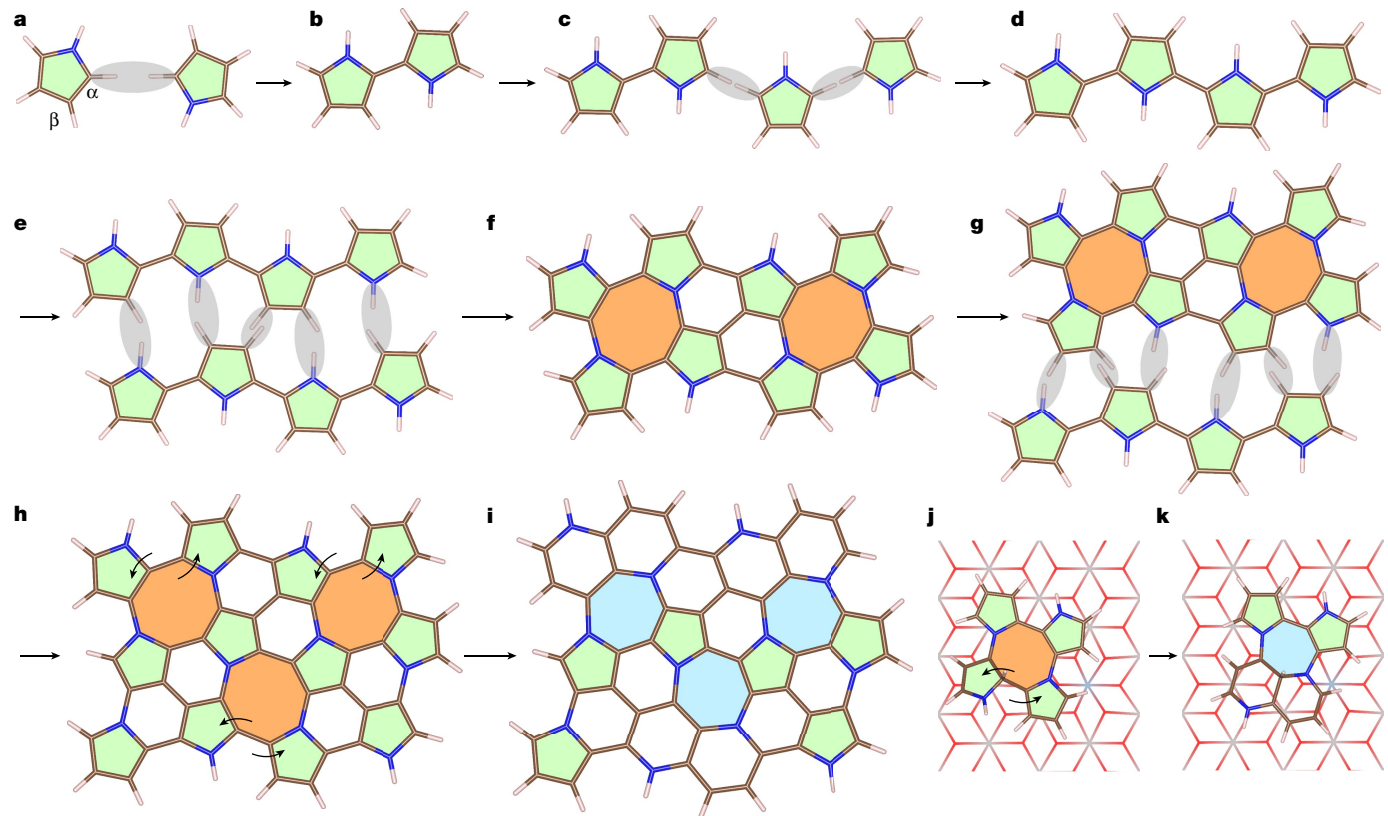


Fig. 2 | The proposed formation process of the NAMC with 5-6-7-membered rings from the pyrrole molecules. **a–d**, Formation of a dimer (**b**) from two pyrrole monomers (**a**) and a one-dimensional chain (**d**) by further polymerization of pyrrole monomers (**c**). **e,f**, Polymerization of two individual one-dimensional chains (**e**) into a dual chain (**f**) through interchain crosslinking. **g,h**, Further polymerization of the dual chain at **f** with another chain (**g**) into a fragment with three chains (**h**). **i**, Final configuration obtained from **h** after the Stone–Wales transformation. **j,k**, Formation of a 5-6-7-membered ring motif (**k**) by

the Stone–Wales transformation from a 5-6-8-membered ring motif (**j**) under the confinement of LDH. The Stone–Wales conversions are marked by black arrows in **h** and **j**. The light grey shadings in **a,c,e** and **g** indicate the sites of the polymerization between either molecules or fragments where the new bonds form. The black arrows indicate the products after the polymerization. H, white; N, blue; C, brown. The LDH is represented with the bond mode, and only the lower layer is shown.

mimicking a highly defective graphene lattice. Note that the 5- and 7-membered rings in our sample always appear as adjoining pairs, denoted as the 5-7 pairs, which is in good agreement with previous theoretical calculations that planar carbon networks could be mosaicked by 5-6-7-membered rings¹⁸ or by only 5-7-membered rings⁶, as the pairing of 5- and 7-membered rings could effectively release the local strain caused by each 5- and 7-membered ring¹⁹. The amorphous structure of NAMC was further confirmed by four-dimensional STEM nanobeam electron diffraction (NBED) analysis (Extended Data Fig. 3), which clearly reveals the absence of single-crystalline graphene domains even at a scale as small as 2 nm, in sharp contrast to nanocrystalline graphene³.

Based on the atomic-number (Z) contrast of STEM-ADF imaging, we can also identify that the atoms with relatively brighter contrast in the two-dimensional network are N atoms (highlighted in Fig. 1e), which was confirmed by atomic-resolution elemental mapping through STEM-EELS spectrum imaging (Fig. 1f and Supplementary Fig. 11). The N content in the NAMC sample, as quantified from the spatial averaged EELS spectrum, is approximately 9 at% (Fig. 1g and Extended Data Fig. 4). Note that the much brighter atoms in the STEM-ADF images (Fig. 1d and Extended Data Fig. 1) are primarily Si contaminants introduced during TEM sample preparation.

The NAMC sample was further characterized by Raman spectroscopy and Fourier transform infrared spectroscopy (FTIR). A new band appears around $1,414\text{ cm}^{-1}$ in the Raman spectra of NAMC (Fig. 1h), presumably resulting from vibrational modes of hexagonal C–N heterocyclic rings^{20,21}, which is absent in conventional polypyrrole (PPy). The FTIR spectrum of NAMC (Supplementary Fig. 12, red line) shows

that the characteristic infrared adsorption peak of the C=C stretching vibration at $1,564\text{ cm}^{-1}$ is red-shifted compared to that of the PPy (Supplementary Fig. 12, blue line), indicating the presence of crosslinking and delocalization in the π -conjugated system. The breathing mode of the pyrrole ring is at $1,170\text{ cm}^{-1}$, and this mode of NAMC is shifted to $1,204\text{ cm}^{-1}$, because the crosslinking increases the rigidity of the rings²². These results clearly indicate that crosslinking occurs during the formation of NAMC.

A synchrotron near-edge X-ray absorption fine structure (NEXAFS) analysis was carried out to determine the chemical state of NAMC. The C K-edge NEXAFS spectrum of NAMC (Supplementary Fig. 13) reveals the dominant feature of sp^2 carbon (285.5 eV)²³ and the presence of a topological structure with 5- and 7-membered rings (283.4 eV)²⁴, which is consistent with the STEM observation (Fig. 1d,e and Extended Data Fig. 2). In addition, the N K-edge NEXAFS spectrum (Fig. 1i) reveals a dominant resonance of graphitic N (at 401.2 eV), with a weak peak around 398.3 eV (ascribed to pyridinic N) and a weak shoulder at 399.6 eV (ascribed to pyrrolic N)²⁵. This indicates that the nitrogen atoms incorporated into the two-dimensional amorphous carbon network are predominantly in the form of graphitic N, whereas a small fraction of pyridinic and pyrrolic N species is also present.

We explored the formation mechanism of 5-6-7-membered rings through crosslinking of the pyrrole molecules using first-principles calculations, as shown in Fig. 2. The calculated interlayer distance of LDH with the intercalation of $S_2O_8^{2-}$ is 8.97 \AA (Supplementary Fig. 14a), consistent with the experimental result of 9.07 \AA , which is larger than for pyrrole monomers (8.41 \AA) (Supplementary Fig. 14b). Thus, after the

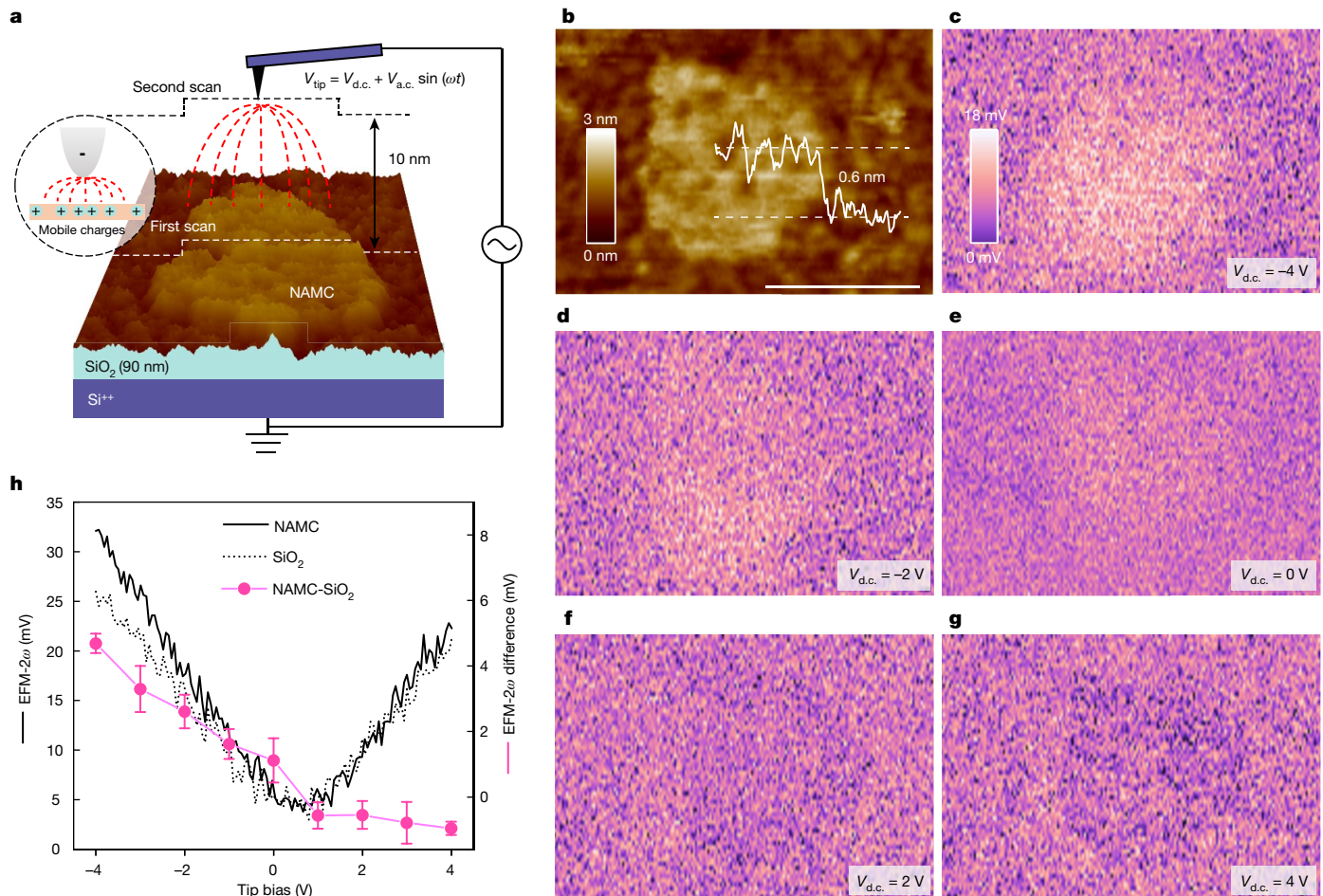


Fig. 3 | Electrical characterization of the NAMC on a SiO_2 substrate by EFM and spectroscopy. **a**, Schematic set-up of EFM. **b**, Topographic image of the NAMC flake. Scale bar, 200 nm. **c–g**, Corresponding EFM- 2ω images at a tip bias ($V_{\text{d.c.}}$) of -4 V (**c**), -2 V (**d**), 0 V (**e**), 2 V (**f**) and 4 V (**g**). The same colour scale is used

in **c–g**. **h**, Representative EFM- 2ω versus $V_{\text{d.c.}}$ spectra acquired on NAMC and the bare SiO_2 substrate, as well as EFM- 2ω contrast between NAMC and the SiO_2 substrate extracted from the mapping mode. Error bars are the standard deviation of the mapping data.

intercalation of $\text{S}_2\text{O}_8^{2-}$, the LDH interlayer could accommodate pyrrole monomers. The pyrrole monomers polymerize preferentially at the Co sites²⁶ (Fig. 2a,b) to form linear oligomers, as shown in Fig. 2c,d. Subjected to the confinement of the LDH, further polymerization occurs through interchain crosslinking at the $\text{C}\beta$ and N sites of two adjacent oligomer chains (Fig. 2e,f), which is significantly different from conventional PPy polymerization dominated by the linking between Ca sites. The bond strength between $\text{C}\beta$ and N is about 0.48 eV weaker than that of α -site coupling (Supplementary Fig. 15); thus, the spatial confinement facilitates the crosslinking reaction. This process proceeds in two dimensions and ultimately produces NAMC (Fig. 2g,h).

The initially formed 5-6-8-membered rings can be converted into 5-6-7-membered rings through the Stone–Wales process^{27,28}, as shown in Fig. 2h,i. The Stone–Wales transformation was examined in detail with a tetramer of pyrrole molecules as an example. The calculated energy barrier for the Stone–Wales transformation under LDH confinement is about 1.12 eV for the tetramer with an extra proton (Fig. 2j,k and Supplementary Fig. 16), much smaller than the corresponding barrier of 3.06 eV without the confinement. Moreover, the Stone–Wales transformation is endothermic by 0.18 eV without the confinement, whereas the process becomes exothermic by -0.17 eV under the confinement subjected to the interaction between the OH groups and the tetramer (Supplementary Fig. 16). Under the confinement of LDH, the buckling of tetramers with 5-8- and 5-6-7-membered rings becomes flattened. Thus, the LDH confinement not only makes the 5-6-7-membered rings thermodynamically more stable but also significantly decreases

the energy barrier for the Stone–Wales transformation from 5-8- to 5-6-7-membered rings. After the Stone–Wales process, the proton detachment from edge N for the 5-6-7-membered rings become exothermic by -0.15 eV with LDH confinement. The characteristics of the adjoining 5-6-7-membered rings from the Stone–Wales process agree well with the STEM images, where pentagon–heptagon pairs are observed (Fig. 1e). Eight-membered rings were occasionally observed in our STEM experiments (Fig. 1d and Extended Data Fig. 1), indicating that 8-membered rings could be an intermediate state. Note that some nitrogen atoms may dissociate from the resulting carbon network during the synthesis of NAMC because of the endothermic nature of incorporating N atoms into the strained, disordered carbon lattice (Extended Data Fig. 5), leading to the reduced N content (compared to that in the pyrrole precursors) and random formation of graphene-like nanodomains, as observed in our experiments.

Given the random distribution of 5-, 6- and 7-membered rings in the 6-membered ring matrix observed in the sample, we constructed a model to mimic the structure displayed in Fig. 1e. Our first-principles calculations show a pseudo-gap of 0.4 eV derived from the highest occupied molecular orbital and the lowest unoccupied molecular orbital, both of which exist as localized states (Extended Data Fig. 6) and resemble those found in amorphous monolayer carbon². The optical bandgap of NAMC, as determined from the Tauc plots²⁹, was 1.92 eV (Extended Data Fig. 7). However, an absorption tail extending to approximately 0.9 eV was observed, which can be attributed to the transitions associated with the localized states, characteristic of amorphous materials^{10,30}.

We used electrostatic force microscopy (EFM) to characterize the electrical properties of the π -conjugated framework of NAMC, as schematically illustrated in Fig. 3a. The non-contact electrical measurement by EFM allows an investigation of the carrier type and concentration of fragile samples while avoiding unintentional contamination and degradation during device fabrication^{31,32}. Figure 3b–g and Supplementary Fig. 17 present the topography and simultaneously obtained EFM- 2ω images of a NAMC flake spin-casted onto a degenerately doped Si substrate with a 90-nm-thick SiO_2 layer. The height profile of approximately 0.6 nm confirms that the NAMC flake is a monolayer. The EFM- 2ω images (Fig. 3c–g) measure the dielectric response, which reflects the charge carrier dynamics of the sample. Note that the contrast between the NAMC flake and the SiO_2 substrate varies as a function of the applied tip voltage ($V_{\text{d.c.}}$). The EFM- 2ω spectra and signals extracted from the mapping mode (Fig. 3h) clearly show that the NAMC film has a higher EFM- 2ω with respect to the SiO_2 substrate at -4 V (Fig. 3c) than at -2 , 0 , 2 or 4 V. This behaviour can be understood by considering that mobile charge carriers in the NAMC flake are subjected to the laterally inhomogeneous electric field of the biased tip^{33,34}. The as-prepared NAMC monolayer should, therefore, be a p-type semiconductor: when the tip voltage is negative, holes in the NAMC film are locally concentrated underneath the tip by electrostatic attraction, yielding an enhanced EFM- 2ω signal relative to the insulating SiO_2 (Fig. 3c). As the tip bias changes from -4 to 0 V, the hole concentration underneath the tip decreases, leading to a reduced EFM- 2ω signal (Fig. 3d,e). The hole concentration in the pristine NAMC film should be very limited; therefore, the monolayer flake appears to be as insulating as the SiO_2 substrate when the tip voltage is zero and for positive tip biases (Fig. 3f,g). The sheet resistance of NAMC deduced from electronic transport measurements is on the level of hundreds of giga-ohms per square (Supplementary Fig. 18). Compared to conventional PPy that requires an extrinsic dopant for electrical conductivity, the presence of 5- and 7-membered rings in the NAMC destroys the symmetry of the hexagonal lattice and disrupts the long-range periodicity of the pristine graphitic network, resulting in variable-range hopping among randomly distributed localized states like that in amorphous carbon^{2,3}.

In summary, we have successfully synthesized NAMC through confined polymerization of N-containing molecules in solution. This graphitic N-doped amorphous carbon may serve as a valuable alternative to N-doped graphene and provide a versatile platform for investigating the correlation between the chemical states of N and the tailored properties of carbon nanomaterials. The confined polymerization strategy can be extended to synthesize two-dimensional amorphous monolayers containing various heteroatoms, as shown by our initial findings for two-dimensional monolayers of PTH (Extended Data Fig. 8) and PCZ (Extended Data Fig. 9). The versatility and wide applicability of this confined growth approach could pave a new avenue to expand the library of two-dimensional amorphous materials.

Online content

Any methods, additional references, Nature Portfolio reporting summaries, source data, extended data, supplementary information, acknowledgements, peer review information; details of author contributions and competing interests; and statements of data and code availability are available at <https://doi.org/10.1038/s41586-024-07958-0>.

- Novoselov, K. S. et al. Electric field effect in atomically thin carbon films. *Science* **306**, 666 (2004).
- Toh, C.-T. et al. Synthesis and properties of free-standing monolayer amorphous carbon. *Nature* **577**, 199–203 (2020).

- Tian, H. et al. Disorder-tuned conductivity in amorphous monolayer carbon. *Nature* **615**, 56–61 (2023).
- Kidambi, P. R., Chaturvedi, P. & Moehring, N. K. Subatomic species transport through atomically thin membranes: present and future applications. *Science* **374**, eabd7687 (2021).
- Castro Neto, A. H., Guinea, F., Peres, N. M. R., Novoselov, K. S. & Geim, A. K. The electronic properties of graphene. *Rev. Mod. Phys.* **81**, 109–162 (2009).
- Crespi, V. H., Benedict, L. X., Cohen, M. L. & Louie, S. G. Prediction of a pure-carbon planar covalent metal. *Phys. Rev. B* **53**, R13303–R13305 (1996).
- Fei, Y. et al. Defective nanographenes containing seven-five-seven (7–5–7)-membered rings. *J. Am. Chem. Soc.* **143**, 2353–2360 (2021).
- Chen, D. et al. Stone-Wales defects preserve hyperuniformity in amorphous two-dimensional networks. *Proc. Natl. Acad. Sci. USA* **118**, e2016862118 (2021).
- Stumm, P., Drabold, D. A. & Fedders, P. A. Defects, doping, and conduction mechanisms in nitrogen-doped tetrahedral amorphous carbon. *J. Appl. Phys.* **81**, 1289–1295 (1997).
- Robertson, J. Amorphous carbon. *Adv. Phys.* **35**, 317–374 (1986).
- Robertson, J. & O'Reilly, E. P. Electronic and atomic structure of amorphous carbon. *Phys. Rev. B* **35**, 2946–2957 (1987).
- Xue, Y. et al. Low temperature growth of highly nitrogen-doped single crystal graphene arrays by chemical vapor deposition. *J. Am. Chem. Soc.* **134**, 11060–11063 (2012).
- Zhang, J. et al. Low-temperature growth of large-area heteroatom-doped graphene film. *Chem. Mater.* **26**, 2460–2466 (2014).
- Leroux, F. & Besse, J.-P. Polymer interleaved layered double hydroxide: a new emerging class of nanocomposites. *Chem. Mater.* **13**, 3507–3515 (2001).
- Lafferré, L. et al. Controlling on-surface polymerization by hierarchical and substrate-directed growth. *Nat. Chem.* **4**, 215–220 (2012).
- Sahabudeen, H. et al. Wafer-sized multifunctional polyimine-based two-dimensional conjugated polymers with high mechanical stiffness. *Nat. Commun.* **7**, 13461 (2016).
- Zhong, Y. et al. Wafer-scale synthesis of monolayer two-dimensional porphyrin polymers for hybrid superlattices. *Science* **366**, 1379–1384 (2019).
- Wang, Z. et al. Phagraphene: a low-energy graphene allotrope composed of 5-6-7 carbon rings with distorted Dirac cones. *Nano Lett.* **15**, 6182–6186 (2015).
- Liu, Y. & Yakobson, B. I. Cones, Pringles, and grain boundary landscapes in graphene topology. *Nano Lett.* **10**, 2178–2183 (2010).
- Do Nascimento, G. M., Constantino, V. R. L. & Temperini, M. L. A. Spectroscopic characterization of doped poly(benzidine) and its nanocomposite with cationic clay. *J. Phys. Chem. B* **108**, 5564–5571 (2004).
- Ayiana, M., Weiss-Hortala, E., Smith, M., McEwen, J.-S. & Garcia-Perez, M. Microstructural analysis of nitrogen-doped char by Raman spectroscopy: Raman shift analysis from first principles. *Carbon* **167**, 559–574 (2020).
- Menon, V. P., Lei, J. & Martin, C. R. Investigation of molecular and supermolecular structure in template-synthesized polypyrrrole tubules and fibrils. *Chem. Mater.* **8**, 2382–2390 (1996).
- Coffman, F. L. et al. Near-edge X-ray absorption of carbon materials for determining bond hybridization in mixed sp^2/sp^3 bonded materials. *Appl. Phys. Lett.* **69**, 568–570 (1996).
- Hua, W., Gao, B., Li, S., Ågren, H. & Luo, Y. X-ray absorption spectra of graphene from first-principles simulations. *Phys. Rev. B* **82**, 155433 (2010).
- Bulushev, D. A. et al. Single isolated Pd^{2+} cations supported on N-doped carbon as active sites for hydrogen production from formic acid decomposition. *ACS Catal.* **6**, 681–691 (2016).
- Sadki, S., Schottland, P., Brodie, N. & Sabouraud, G. The mechanisms of pyrrole electropolymerization. *Chem. Soc. Rev.* **29**, 283–293 (2000).
- Ertkin, E., Chrzan, D. C. & Daw, M. S. Topological description of the Stone-Wales defect formation energy in carbon nanotubes and graphene. *Phys. Rev. B* **79**, 155421 (2009).
- Ma, J., Alfè, D., Michaelides, A. & Wang, E. Stone-Wales defects in graphene and other planar sp^2 -bonded materials. *Phys. Rev. B* **80**, 033407 (2009).
- Tauc, J., Grigorovici, R. & Vancu, A. Optical properties and electronic structure of amorphous germanium. *Phys. Status Solidi B Basic Solid State Phys.* **15**, 627–637 (1966).
- Tauc, J. Optical properties and electronic structure of amorphous Ge and Si. *Mater. Res. Bull.* **3**, 37–46 (1968).
- Zhang, J., Lu, W., Li, Y. S., Cai, J. & Chen, L. Dielectric force microscopy: imaging charge carriers in nanomaterials without electrical contacts. *Acc. Chem. Res.* **48**, 1788–1796 (2015).
- Yang, Y. et al. Probing nanoscale oxygen ion motion in memristive systems. *Nat. Commun.* **8**, 15173 (2017).
- Jiang, Y. et al. Direct observation and measurement of mobile charge carriers in a monolayer organic semiconductor on a dielectric substrate. *ACS Nano* **5**, 6195–6201 (2011).
- Gildemeister, A. E. et al. Measurement of the tip-induced potential in scanning gate experiments. *Phys. Rev. B* **75**, 195338 (2007).

Publisher's note Springer Nature remains neutral with regard to jurisdictional claims in published maps and institutional affiliations.

Springer Nature or its licensor (e.g. a society or other partner) holds exclusive rights to this article under a publishing agreement with the author(s) or other rightsholder(s); author self-archiving of the accepted manuscript version of this article is solely governed by the terms of such publishing agreement and applicable law.

© The Author(s), under exclusive licence to Springer Nature Limited 2024, corrected publication 2024

Methods

Synthesis of the NAMC

Free-standing NAMC was fabricated with a space-confined synthesis method using layered NiAl-LDH as the removable templates. First, single-crystal Ni/Al-LDH templates were synthesized. $\text{Ni}(\text{NO}_3)_2 \cdot 6\text{H}_2\text{O}$ (0.47 mmol), $\text{Al}(\text{NO}_3)_3 \cdot 9\text{H}_2\text{O}$ (0.23 mmol) and hexamethylenetetramine (3 mmol) were dissolved in deionized water (30 ml). The mixture was stirred for 0.5 h at room temperature and then transferred to a Teflon-lined stainless-steel autoclave. The autoclave was sealed and maintained at 473 K for 24 h and then cooled to room temperature. The resulting turquoise product was collected through centrifugation and rinsed three times with water and finally dried under vacuum. Large Mg/Al LDHs were synthesized through a similar hydrothermal process. $\text{Mg}(\text{NO}_3)_2 \cdot 6\text{H}_2\text{O}$ (2.5 mmol), $\text{Al}(\text{NO}_3)_3 \cdot 9\text{H}_2\text{O}$ (1.25 mmol) and urea (12.65 mmol) were dissolved in deionized water (25 ml) and transferred to a Teflon-lined stainless-steel autoclave. The autoclave was sealed and maintained at 383 K for 24 h.

Second, $(\text{NH}_4)_2\text{S}_2\text{O}_8$ (0.22 mmol) was dissolved in deionized water (50 ml) at a low temperature of 275 K to avoid spontaneous decomposition. The as-prepared LDHs were ultrasonically dispersed into deionized water (30 ml) and then added to the $(\text{NH}_4)_2\text{S}_2\text{O}_8$ solution. The mixed solution was continuously stirred for 24 h at 275 K to guarantee sufficient anion exchange of $\text{S}_2\text{O}_8^{2-}$ with the interlayered anions of LDHs. The $\text{S}_2\text{O}_8^{2-}$ -intercalated LDHs were collected and rinsed with deionized water to remove the excess $\text{S}_2\text{O}_8^{2-}$ on the surfaces of LDHs, which was also removed from the aqueous solution. The resulting product was redispersed in 80 ml deionized water at 275 K for further polymerization.

Finally, pyrrole (0.7 mmol) was dissolved in ethanol (5 ml). The pyrrole solution was added into the as-prepared mixture drop by drop, followed by continuous stirring for 10 h at 275 K. The resulting black product was collected through centrifugation and rinsed three times with ethanol and then kept in deionized water (10 ml) as the suspension. Finally, the above suspension was put in 1 M HCl aqueous solution and stirred for 12 h to remove the LDH template. The resulting product was collected through centrifugation, rinsed three times with water and kept in ethanol (10 ml) for testing. In addition, PPy samples were synthesized under the same conditions without the LDH templates for comparison.

Synthesis of the two-dimensional monolayer PTH

The two-dimensional monolayer PTH was fabricated by a similar confined synthesis method using layered NiAl-LDHs as removable templates. The synthesis procedure of the NiAl-LDH is identical to that described above. Second, $(\text{NH}_4)_2\text{S}_2\text{O}_8$ (0.37 mmol) was dissolved in deionized water (50 ml). The as-prepared LDHs were ultrasonically dispersed into deionized water (30 ml) and then added to the $(\text{NH}_4)_2\text{S}_2\text{O}_8$ solution. The mixed solution was continuously stirred for 4 h at 275 K. The $\text{S}_2\text{O}_8^{2-}$ -intercalated LDHs were collected and rinsed with deionized water to remove the excess $\text{S}_2\text{O}_8^{2-}$ on the surfaces of LDHs, which was also removed from the aqueous solution. The resulting product was redispersed in deionized water (65 ml) at 275 K for further polymerization. Finally, thiophene (1.90 mmol) was dissolved in ethanol (20 ml) and added dropwise into the as-prepared $\text{S}_2\text{O}_8^{2-}$ -intercalated NiAl-LDHs solution, which was followed by continuous stirring for 10 h at 343 K under condensation reflux. The subsequent template etching and washing procedures are identical to those for NAMC.

Synthesis of the two-dimensional monolayer PCZ

The two-dimensional PCZ was fabricated by a similar confined synthesis method using layered NiAl-LDH as removable templates. The synthesis procedure of the NiAl-LDH is identical to that described above. Second, $(\text{NH}_4)_2\text{S}_2\text{O}_8$ (0.09 mmol) was dissolved in deionized water (50 ml). The as-prepared LDHs were ultrasonically dispersed into deionized water

(30 ml) and then added to the $(\text{NH}_4)_2\text{S}_2\text{O}_8$ solution. The mixed solution was continuously stirred for 4 h at 275 K. The $\text{S}_2\text{O}_8^{2-}$ -intercalated LDHs were collected and rinsed with deionized water to remove the excess $\text{S}_2\text{O}_8^{2-}$ on the surfaces of LDHs, which was also removed from the aqueous solution. The resulting product was redispersed in deionized water (80 ml) at 275 K for further polymerization. Finally, carbazole (0.03 mmol) was dispersed in ethanol (5 ml) by ultrasonication. The carbazole solution was added into the as-prepared $\text{S}_2\text{O}_8^{2-}$ -intercalated LDHs mixture drop by drop, which was followed by continuous stirring for 10 h at 275 K. The subsequent template etching and washing procedures are identical to those for NAMC.

Sample characterization

Raman spectra were acquired with a Jobin Yvon Raman spectrometer model HR800 (laser wavelength, 633 nm; power, 0.8 mW; acquisition time, 10 s; samples were transferred onto SiO_2 substrates before spectra were acquired). Powder X-ray diffraction analysis of the samples was performed using a Shimadzu Xlab6000 X-ray diffractometer. The data were collected in Bragg–Brentano mode with a scan rate of 5° min^{-1} . The N K-edge and C K-edge NEXAFS data were obtained at the BL10B beamline of the National Synchrotron Radiation Laboratory (China) under the total-electron-yield mode with vacuum better than 1×10^{-7} Pa. FTIR spectra were collected using a Thermo Nicolet nexus-470 FTIR instrument. X-ray photoelectron spectroscopy data were recorded with a Thermo Scientific ESCALAB 250 Xi XPS system. The analysis chamber was at 1.5×10^{-9} mbar, and the lateral size of the X-ray spot was 500 μm . All spectra were referenced to the C 1s binding energy of 284.8 eV. AFM analysis was performed in tapping mode in air with a Dimension Icon (Bruker). OTESPA (Olympus AC160TS-10 AFM tip) tips were used. The optical images were taken by an optical microscope (Olympus bx53m). Electron paramagnetic resonance spectra were recorded on a Bruker E500 spectrometer at 275 K, with a modulation amplitude, modulation frequency and microwave power of 1 G, 100 kHz and 1 mW. Inductively coupled plasma atomic emission spectroscopy was carried out on an Agilent 725ES instrument.

Electron microscopy

The NAMC samples were ultrasonically dispersed in ethanol and transferred onto a copper grid for TEM measurements. TEM imaging, selected-area electron diffraction and energy-dispersive spectroscopy analyses were carried out on a JEOL-2100F operating at 200 kV. Aberration-corrected STEM imaging and EELS mapping were performed on a Nion HERMES-100 microscope under an accelerating voltage of 60 kV. Before a test, the sample was baked in vacuum at 373 K for 10 h. ADF images were acquired with a 32 mrad convergence angle, a 15 pA probe current and a collection angle range of 44–210 mrad. The high-angle ADF images with a collection angle range of 75–210 mrad were acquired simultaneously with EELS spectrum imaging. EELS was performed under the same setting with a collection angle of about 75 mrad. The atomic ADF images were processed by a double Gaussian filter³⁵ to remove the electron-probe-tail effect and to enhance the contrast of N atoms. EELS images were denoised by principal component analysis using the open Python package Hyperspy³⁶. The energy-loss range chosen for the principal component analysis was 250–450 eV. The first three components were chosen to reconstruct the denoised data based on their mathematical significance. The convergence semi-angle and beam current for the four-dimensional STEM NBED experiment were 2 mrad and 6 pA, respectively. The NBED datasets were acquired over 32 nm × 32 nm regions of the samples, with a scanning step of 0.25 nm and an exposure time of 10 ms for NAMC samples (Extended Data Fig. 3) or a scanning step of 2 nm and an exposure time of 2 s for two-dimensional monolayer PTH and PCZ samples (Extended Data Figs. 8g–k and 9g–k). The NBED dataset was processed by the open Python package pyxem³⁷. The morphologies were observed using a JEOL JSM-7500F field-emission scanning electron microscope.

EFM characterizations

The NAMC samples were ultrasonically dispersed in ethanol and drop-casted onto a n-doped Si(100) substrate with a 90 nm SiO₂ layer. All EFM experiments were carried out on a commercial scanning probe microscope (Dimension Icon, Bruker) operating under a dual pass tapping mode. On the first pass, the topographic image was obtained without applying any voltage between the probe and the sample. On the second pass, an external bias, $V_{\text{tip}} = V_{\text{d.c.}} + V_{\text{a.c.}} \sin(\omega t)$ ($V_{\text{a.c.}}$, $\sin(\omega t)$ is the modulation voltage), was applied to the Pt/Ir-coated silicon probe (SCM-PIT-V2, Bruker) as it was lifted by a constant height $z = 10$ nm above the sample surface. For all the EFM measurements, $V_{\text{a.c.}}$ was set to 1 V with a modulation frequency of 1 kHz. The phase shift signal of the cantilever was fed into two lock-in amplifiers to demodulate the 1ω and 2ω components. The EFM- 1ω and EFM- 2ω signals were fed back into the AFM controller simultaneously through a signal access module.

Computational set-up

The Vienna Ab Initio Simulation Package (VASP)³⁸ was used for first-principles calculations. The generalized gradient approximation of the Perdew–Burke–Ernzerhof functional³⁹ was used to describe the commutative correlation energy except where noted. A Hubbard U term was applied to the Ni 3d orbitals of LDH systems with the U value set to 5.5 eV (ref. 40). For all calculations, the kinetic energy cutoff of the plane wave was 500 eV. Grimme D3 corrections was used to describe the van der Waals interactions⁴¹. The vacuum zone was set to 10 Å to avoid interactions between periodic replicas. Gamma only was used for the k -point sampling considering that it was a larger system. The structure relaxes until the force on each atom is less than 0.01 eV Å⁻¹. The convergence criterion of electron iteration was 10^{-6} eV. The energy barrier of the Stone–Wales transformation was simulated with a nudged elastic band for one tetramer under the confinement of a (4 × 4) LDH supercell.

Data availability

Source data are provided with this paper. All other data are available in the main text or the Supplementary Information.

35. Krivanek, O. L. et al. Atom-by-atom structural and chemical analysis by annular dark-field electron microscopy. *Nature* **464**, 571–574 (2010).
36. Francisco, D. L. P. et al. Hyperspy/hyperspy: Release v1.6.2 (HyperSpy, 2021).
37. Clausen, A. et al. LiberTEM: software platform for scalable multidimensional data processing in transmission electron microscopy. *J. Open Source Softw.* <https://doi.org/10.21105/joss.02006> (2020).
38. Kresse, G. & Furthmüller, J. Efficiency of ab-initio total energy calculations for metals and semiconductors using a plane-wave basis set. *Comput. Mater. Sci.* **6**, 15–50 (1996).
39. Perdew, J. P., Burke, K. & Ernzerhof, M. Generalized gradient approximation made simple. *Phys. Rev. Lett.* **77**, 3865–3868 (1996).
40. Tkalych, A. J., Zhuang, H. L. & Carter, E. A. A density functional + U assessment of oxygen evolution reaction mechanisms on β -NiOOH. *ACS Catal.* **7**, 5329–5339 (2017).
41. Grimme, S., Ehrlich, S. & Goerigk, L. Effect of the damping function in dispersion corrected density functional theory. *J. Comput. Chem.* **32**, 1456–1465 (2011).

Acknowledgements This work was financially supported by the National Natural Science Foundation of China (Grant Nos. 51532001, 52225308, 11974037, 22372048, 61327813, 51802053 and 52025025), the National Key R&D Programme (Grant No. 2017YFA0205000), the Strategic Priority Research Programme of the Chinese Academy of Sciences (Grant No. XDB36000000), the Royal Society’s Newton Advanced Fellowship scheme (Grant No. NAF/R1/180242), the Beijing Outstanding Young Scientist Programme (Grant No. BJWZYLH01201914430039) and the Chinese Academy of Sciences Project for Young Scientists in Basic Research (Grant No. YSBR-003). This research benefited from the resources and support of the Electron Microscopy Center at the University of Chinese Academy of Sciences. We thank BL10B and BL12B in the National Synchrotron Radiation Laboratory for characterizations by synchrotron radiation. We thank Y. Li for helpful discussions and suggestions.

Author contributions L. Guo and X.Q. proposed and supervised the project. X.B., P.H., Y.Z., T.J., Z.W. and H.C. prepared the samples and spectroscopy characterization. Ang L., Aowen L., L. Gu and W.Z. performed the STEM characterization and analysis. Y.X. conducted the theoretical calculations. G.Z. performed the EFM measurements and analysis. J.K. and H.Z. carried out the soft X-ray absorption spectroscopy experiments. L. Guo, L.L., W.Z., X.Q. and L. Gu analysed data and wrote the manuscript. All authors discussed the results and commented on the manuscript. X.B., P.H., Ang L., Y.Z., Aowen L., G.Z. and Y.X. contributed equally to this work.

Competing interests The authors declare no competing interests.

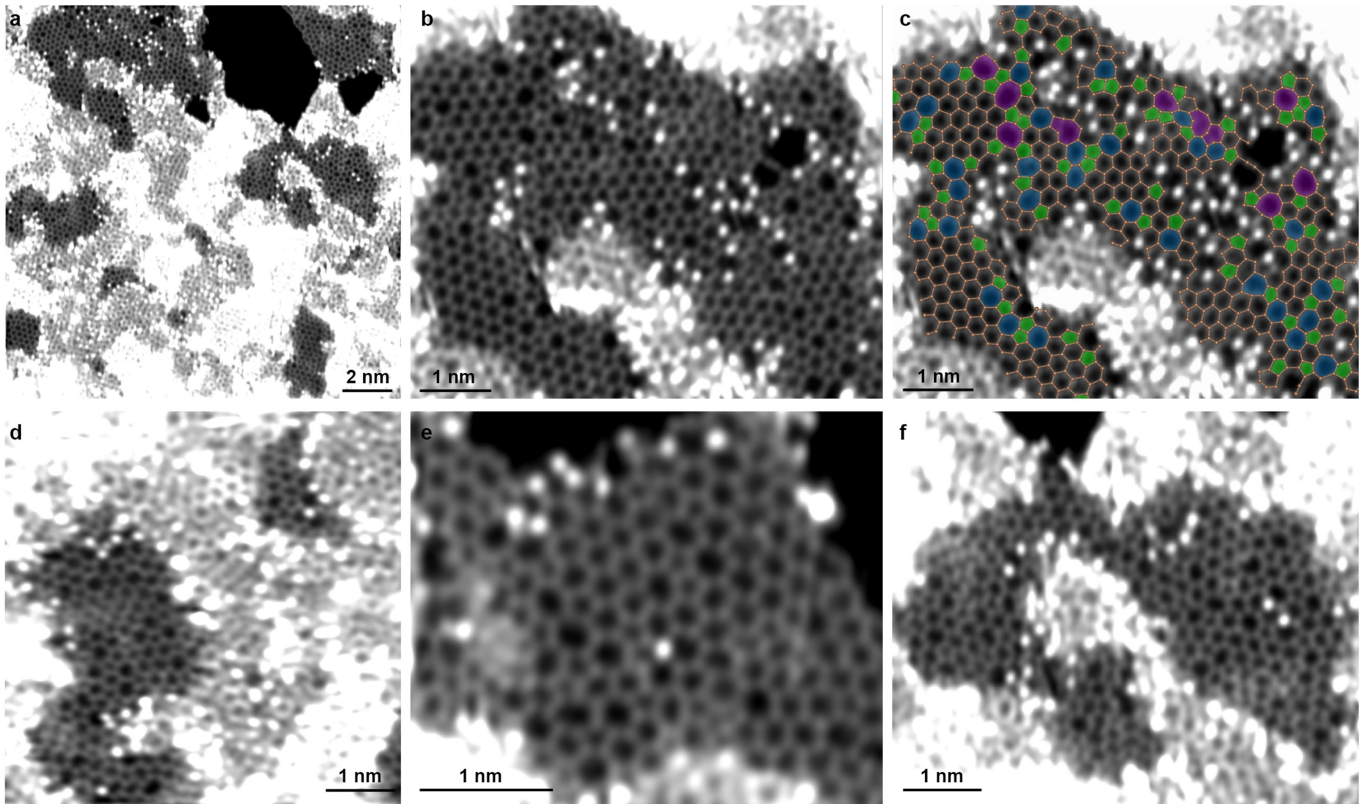
Additional information

Supplementary information The online version contains supplementary material available at <https://doi.org/10.1038/s41586-024-07958-0>.

Correspondence and requests for materials should be addressed to Lin Gu, Wu Zhou, Li-Min Liu, Xiaohui Qiu or Lin Guo.

Peer review information *Nature* thanks Dongmok Whang and Federico Rosei and the other, anonymous, reviewer(s) for their contribution to the peer review of this work. Peer reviewer reports are available.

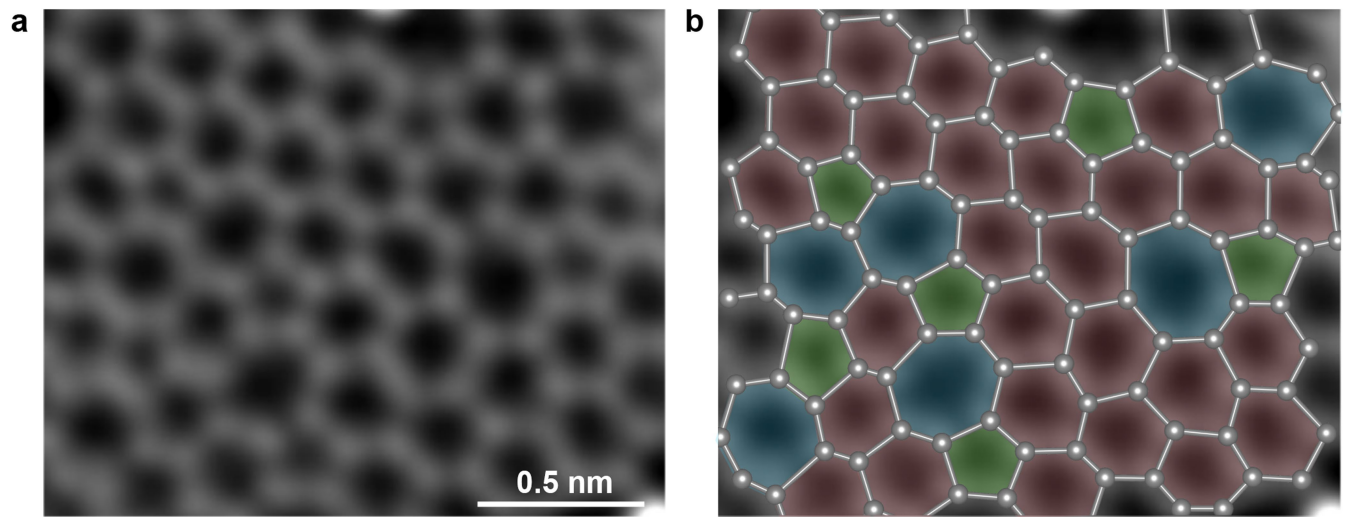
Reprints and permissions information is available at <http://www.nature.com/reprints>.



Extended Data Fig. 1 | Additional STEM-ADF images of the NAMC sample.

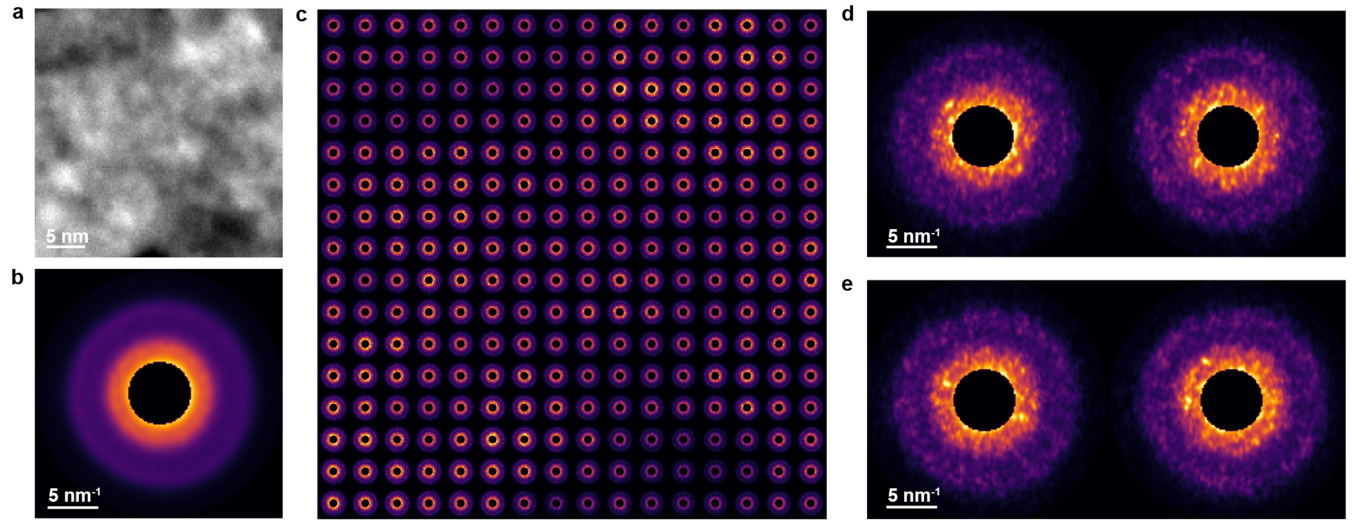
a, Larger field of view STEM-ADF image of NAMC (field of view $16 \text{ nm} \times 16 \text{ nm}$).
b, STEM-ADF image of NAMC, showing a highly disorder atomic arrangement distinctly different from nanocrystalline graphene (field of view $6.6 \text{ nm} \times 5.6 \text{ nm}$). This image is duplicate of Fig. 1d of the main text.
c, Overlay of the schematic atomic structure model on the atomic resolution STEM-ADF image in

b. The 5-, 7- and 8-membered rings are highlighted with green, blue and purple, respectively. The bright atoms are impurity atoms introduced during the removal of the LDH template and TEM sample preparation. **d-f**, Additional atomic resolution STEM-ADF images of NAMC, all showing an amorphous structure. Pin-holes and small restacking nano-flakes can be observed from the images.



Extended Data Fig. 2 | Aberration-corrected STEM-HAADF image of NAMC with the five-, six- and seven- membered rings structure crosslinked by pyrrole rings. a, Aberration-corrected STEM-HAADF image processed by a

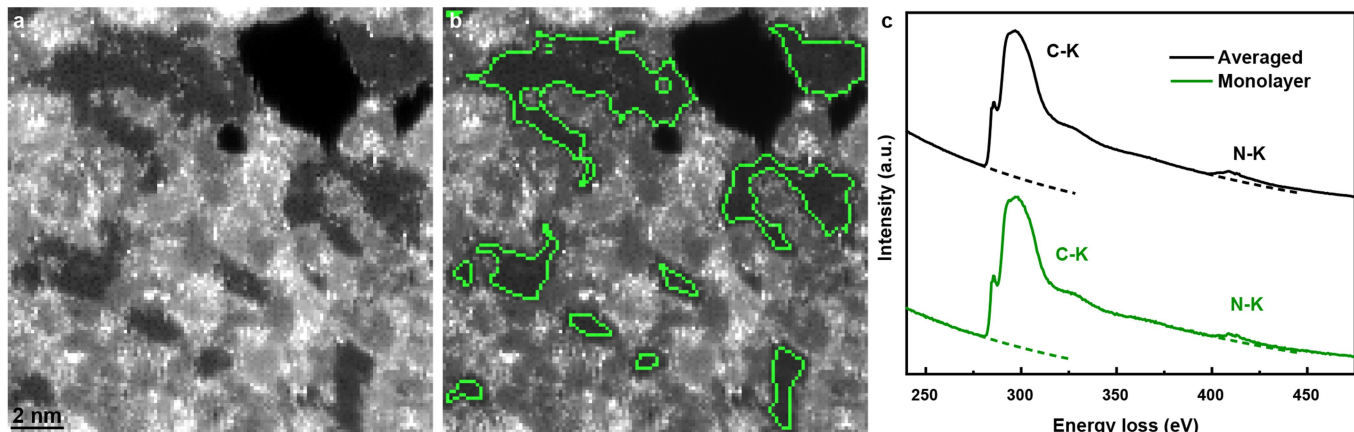
double-gaussian filter. **b,** A color overlay is added for identification of 5- (green), 6- (pink) and 7- (blue) membered rings.



Extended Data Fig. 3 | 4D-STEM NBED characterization of NAMC. **a**, STEM image of a multilayer thin flake of NAMC. **b**, Summed NBED pattern of the whole area in **a** over an area of $32 \text{ nm} \times 32 \text{ nm}$, showing diffuse halos. **c**, Array of the summed NBED patterns of the 16×16 subregions of **a** (The size of each subregion

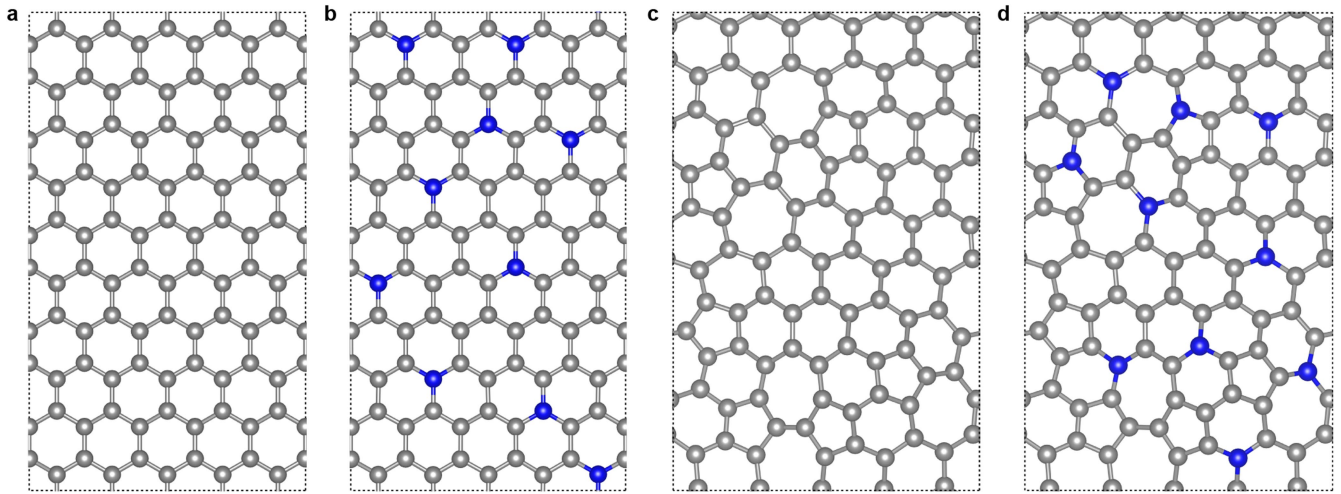
is $2 \text{ nm} \times 2 \text{ nm}$). **d**, **e**, Two representative pairs of adjacent NBED patterns in **c**, indicating that the sample features a highly disordered structure even at a scale as small as $2 \text{ nm} \times 2 \text{ nm}$.

Article



Extended Data Fig. 4 | STEM-EELS analysis of the NAMC sample. **a**, The simultaneously acquired STEM-HAADF image of the sample area for STEM-EELS mapping (the same area as shown in Extended Data Fig. 1a). **b**, Same image as **a** with the contours of the monolayer regions marked with the green lines. Apart from the highlighted monolayer regions and pinholes, this sample area contains primarily re-stacked bilayers. **c**, The EELS spectra summed over the whole

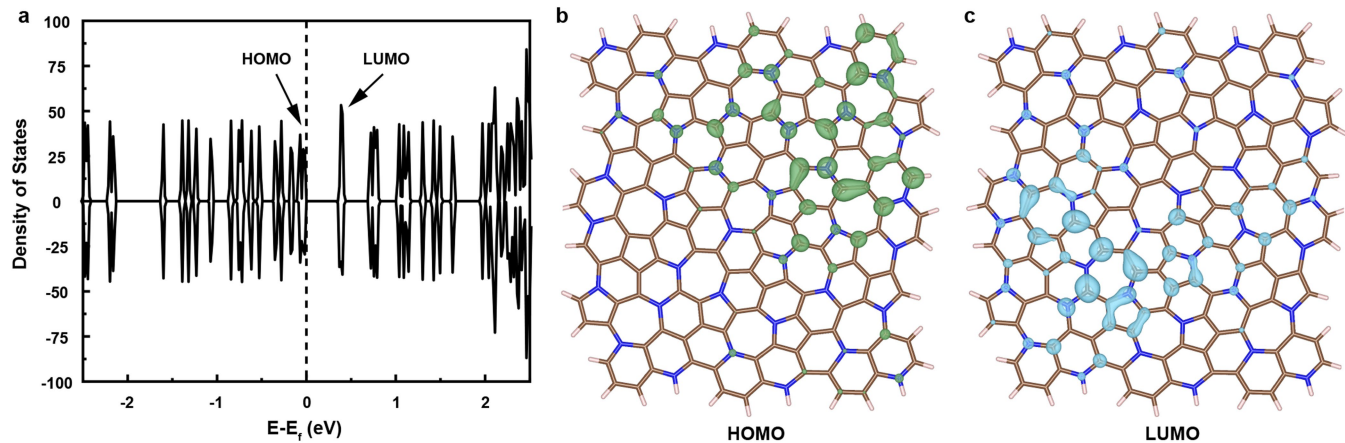
dataset (black) and the monolayer regions (green), both showing a similar nitrogen content of ~9%. The agreement of N content in both of monolayer regions and the overall sample indicates the measured N signal comes from the N atoms incorporated into the 2D amorphous carbon network, precluding the possible contribution of N species adsorbed on the surface or in contaminants.



Extended Data Fig. 5 | Structural models for formation energy calculations of N doping in graphene and amorphous monolayer carbon. **a, b,** Structural models for graphene (**a**) and N-doped graphene (**b**). **c, d,** Structural models for amorphous monolayer carbon (**c**) and NAMC (**d**). Blue and grey balls stand for N and C atoms, respectively. The formation energy of N-doping atoms was calculated by the equation: $E_f = E_{\text{N-doped}} - E_{\text{pure}} - nE_N + nE_C$, where $E_{\text{N-doped}}$ and E_{pure} represent the total energies of the N-doped structure and the pristine structure, respectively. E_N and E_C correspond to the energy per N atom in N_2 gas and the energy per C atom in graphene, respectively. Meanwhile, n stands for the total

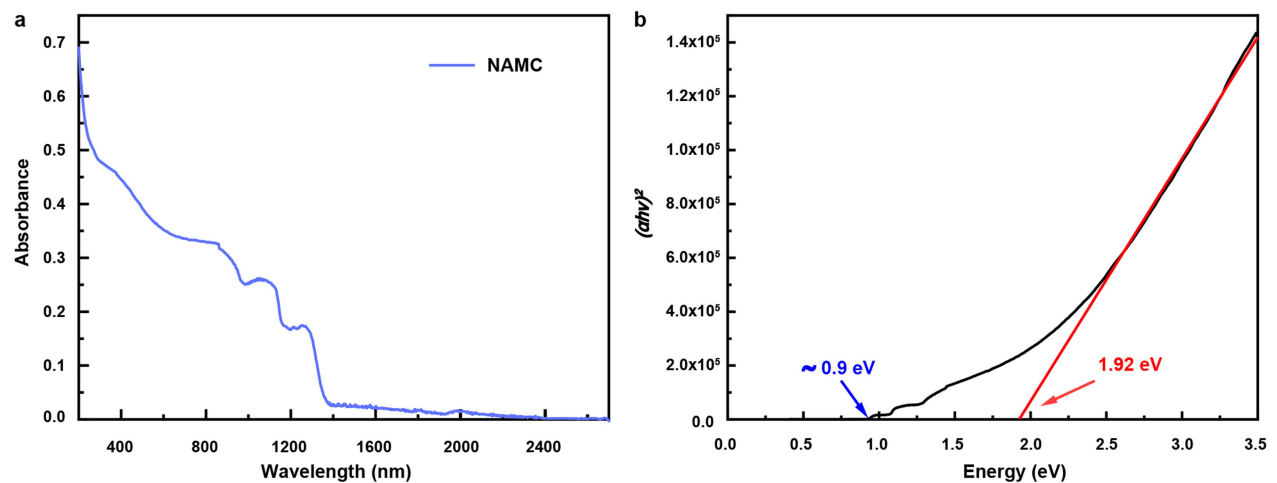
number of doping atoms. The pristine structural model for either graphene or amorphous monolayer carbon contains 100 C atoms, and the N-doped model contains 90 C atoms and 10 N atoms, corresponding to 10 at% N doping in both graphene and amorphous monolayer carbon. First-principles calculations indicate that the formation energy of N doping in amorphous monolayer carbon is lowered to 0.60 eV per N as compared to that of N-doped graphene (0.92 eV per N), making it potentially easier to incorporate nitrogen into the strained disordered carbon lattice.

Article

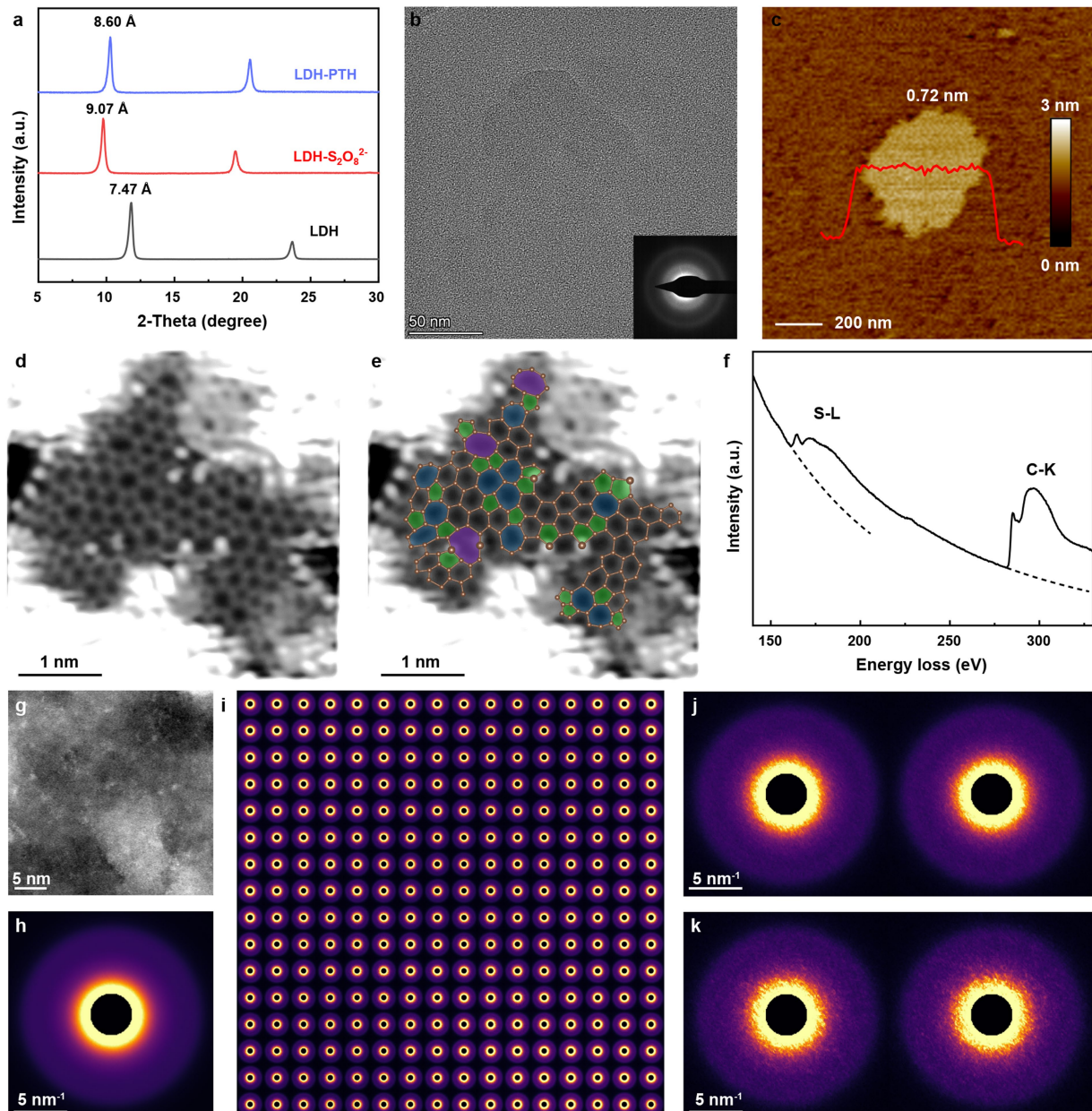


Extended Data Fig. 6 | Calculated electronic structures of NAMC with a planer model structure using HSE06 functional. **a**, Density of states. There is a pseudo-gap of 0.4 eV between the highest occupied molecule orbital (HOMO) and the lowest unoccupied molecule orbital (LUMO). **b, c**, Illustration

of HOMO (**b**) and LUMO (**c**), respectively. The size of the model structure is about $20 \text{ \AA} \times 20 \text{ \AA}$, consisting of the 5-, 6- and 7- rings. The isosurface is $0.0015 \text{ e}/\text{\AA}^3$. H: white, C: brown, N: blue.

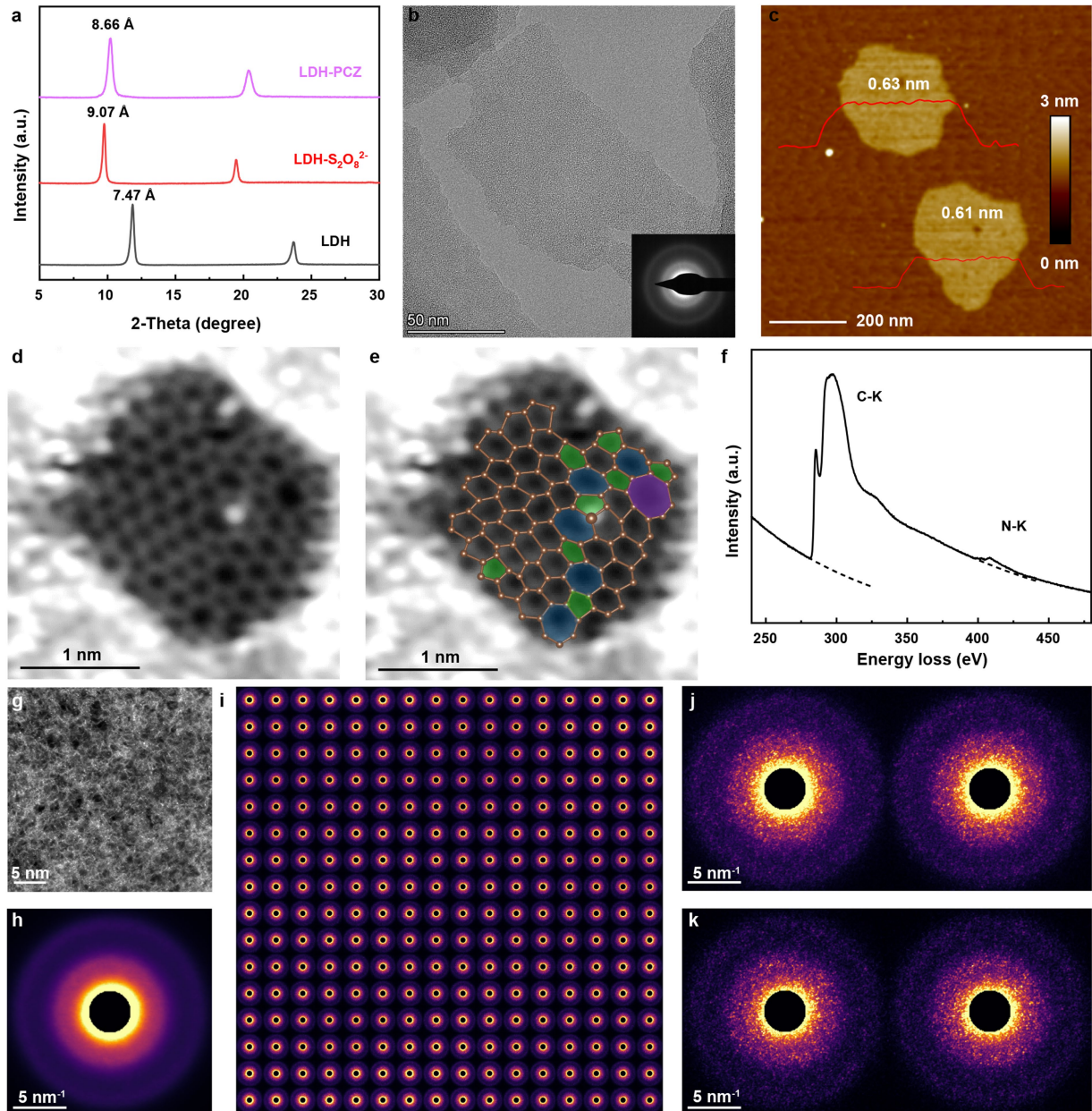


Extended Data Fig. 7 | Optical bandgap measurement of NAMC. **a**, UV-Vis-NIR absorption spectrum of NAMC. **b**, Tauc plots derived from the absorption spectrum. The red line indicates linear extrapolation of the absorption edge.



Extended Data Fig. 8 | Characterizations of the 2D monolayer PTH. **a**, XRD profiles of LDH, LDH-S₂O₈²⁻ and LDH-PTH. Similar to the ion-exchange and confined polymerization process of NAMC, the interlayer distance of LDH increases from 7.47 Å to 9.07 Å after the intercalation of S₂O₈²⁻, and shrinks to 8.60 Å upon the decomposition of S₂O₈²⁻ to produce LDH-PTH. **b**, TEM image and SAED pattern of PTH. **c**, AFM image and the corresponding height profile of monolayer PTH. **d**, Atomic resolution STEM-ADF image of monolayer PTH. **e**, Overlay of the schematic atomic structural model on **d**. The 5-, 7- and 8-membered rings are highlighted with green, blue and purple, respectively.

f, EELS spectrum acquired over a 32 nm × 32 nm sample area. The S content is approximately 6% as quantified from the EELS spectrum. **g**, STEM-ADF image of a PTH nanosheet. **h**, Summed NBED pattern of the whole area in **g** over an area of 32 nm × 32 nm, showing diffuse halos characteristic of an amorphous structure. **i**, Array of the NBED patterns of the 16 × 16 subregions of **g**. The size of each subregion is 2 nm × 2 nm. **j**, **k**, two representative pairs of adjacent NBED patterns in **i**, all showing diffuse halos, suggesting that the sample features a highly disordered structure even at a scale as small as 2 nm × 2 nm.



Extended Data Fig. 9 | Characterizations of the 2D monolayer PCZ. **a**, XRD profiles of LDH, LDH-S₂O₈²⁻ and LDH-PCZ. Similar to the ion-exchange and confined polymerization process of NAMC, the interlayer distance of LDH increases from 7.47 Å to 9.07 Å after the intercalation of S₂O₈²⁻, and shrinks to 8.66 Å upon the decomposition of S₂O₈²⁻ to produce LDH-PCZ. **b**, TEM image and SAED pattern of PCZ. **c**, AFM image and the corresponding height profile of monolayer PCZ. **d**, Atomic resolution STEM-ADF image of monolayer PCZ. **e**, Overlay of the schematic atomic structural model on **d**. The 5-, 7- and 8-membered rings are highlighted with green, blue and purple, respectively.

f, EELS spectrum acquired over a 32 nm × 32 nm sample area. The N content is approximately 4% as quantified from the EELS spectrum. **g**, STEM-ADF image of a PCZ nanosheet. **h**, Summed NBED pattern of the whole area in **g** over an area of 32 nm × 32 nm, showing diffuse halos characteristic of an amorphous structure. **i**, Array of the NBED patterns of the 16 × 16 subregions of **g**. The size of each subregion is 2 nm × 2 nm. **j**, **k**, two representative pairs of adjacent NBED patterns in **i**, all showing diffuse halos, suggesting that the sample features a highly disordered structure even at a scale as small as 2 nm × 2 nm.